Journal of Electronic Materials (2024) 53:5007–5017
https://doi.org/10.1007/s11664-024-11063-3

28TH INTERNATIONAL CONFERENCE ON NUCLEAR TRACKS AND RADIATION MEASUREMENTS

Modification of the Properties of Titanium Carbide MXene by Ag Doping via Ion Implantation for Quantum Dot-Sensitized Solar Cell Applications

Iqbal Singh[1] · Devrani Devi[2] · Fouran Singh[2] · Sundeep Chopra[2] · Aman Mahajan[1]

Received: 29 December 2023 / Accepted: 22 March 2024 / Published online: 20 April 2024

Abstract

The current work investigates ion implantation of a transition metal (Ag) into MXene/TiO_2 films utilizing low energy at different fluence rates of 5×10^{12}, 5×10^{13}, 5×10^{14}, and 5×10^{15} ions-cm^{-2} respectively. The morphology and crystal structure of the transition metal-implanted MXene/TiO_2 samples were characterized by field-emission scanning electron microscopy, x-ray diffraction, and Raman spectroscopy. In addition, x-ray photoelectron spectroscopy revealed the presence of Ag(I) oxidation state at 5×10^{14} ions-cm^{-2} fluence, whereas at a higher fluence of 5×10^{15} ions-cm^{-2}, both Ag(I) and Ag(0) states were found. The optical properties of the transition metal-implanted MXene/TiO_2 samples were also investigated via UV-visible and photoluminescence studies. The transition metal implantation significantly enhanced the light absorption and reduced the charge recombination owing to the formation of defect states. Finally, the quantum dot-sensitized solar cell (QDSSC) device fabricated with 5×10^{14} ions-cm^{-2} (Ag_3) exhibited the highest power conversion efficiency of 3.94% versus the unimplanted MXene/TiO_2-based QDSSC (2.48%), which is attributed to enhanced absorption and minimization of charge recombinations, as confirmed by photovoltaic characteristics and Nyquist plots.

Keywords QDSSC · ion implantation · light harvesting · TiO_2

Introduction

Third-generation quantum dot-sensitized solar cells (QDSSCs) have attracted significant interest due to their economical production, streamlined manufacturing processes, and their ability to operate efficiently even under low illumination.[1] QDSSCs can be conceptually considered an evolutionary extension of conventional dye-sensitized solar cells (DSSCs). Nonetheless, in QDSSCs, quantum dots (QDs) are employed as a sensitizer in place of organic dyes, as QDs have exceptional properties including a tunable band gap, multiple exciton generation, and high extinction coefficient, which make the solar cells more efficient.[2] QDSSCs typically comprise a photoanode made of TiO_2 as an electron transport layer (ETL) sensitized with quantum dots, a polysulfide electrolyte as a hole transport layer (HTL), and a counter electrode (CE) composed of Cu_2S@brass.[3]

A conventional mesoporous TiO_2 (m-TiO_2)-based photoanode still suffers from various limitations, such as low light harvesting because of the wide band gap of TiO_2, and sluggish charge transport dynamics and numerous recombinations owing to the large grain boundaries of m-TiO_2. The light harvesting of the m-TiO_2 photoanode can be enhanced by scattering the incoming light or, alternatively, expanding the absorption spectrum of the photoanode, enabling it to capture a wider spectrum of wavelengths. Further, electron-hole recombinations can be reduced by establishing a more efficient transport network, facilitating the swift movement of electrons to the electrode. Additionally, creating new trap levels in the material can prevent electron–hole recombination, helping in the separation of charge carriers.[4]

The use of large nanostructures in the photoanode can effectively scatter incoming light, leading to an improved

✉ Aman Mahajan
aman.phy@gndu.ac.in

[1] Material Science Laboratory, Department of Physics, Guru Nanak Dev University, Amritsar 143005, India

[2] Inter University Accelerator Centre, New Delhi 110 0067, India

light harvesting mechanism through the Mie scattering phenomena.[5] In this direction, different large-sized nanostructures, including large nanoparticles,[6] nanofibers,[7] nanobeads,[8] nanorods,[9] and nanotubes,[10] have been employed as effective light scatterers. Moreover, doping of the photoanode with noble metals such as Au, Ag, and Cu helps to broaden the absorption spectra through the induction of local surface plasmon resonance (LSPR) effects.[11,12] Also, noble metal doping induces new impurity states positioned between the conduction band and valance band of TiO_2, serving the dual purpose of facilitating enhanced absorption at higher wavelengths and functioning as centers for charge separation, thereby mitigating the occurrence of charge recombination.[13] In this context, Raguram et al.[14] demonstrated a reduction in the band gap of TiO_2 through Cu doping, leading to an improvement in current density values. Dong et al.[15] reported a 22% enhancement in efficiency for a photoanode based on Ag-TiO_2, attributing it to the broadening of absorption edges.

Recently, a two-dimensional (2D) titanium carbide-based MXene ($Ti_3C_2T_x$) has gained considerable attention in photovoltaic technology owing to its efficient intrinsic properties, such as high electrical conductivity, thermal stability, and hydrophilic nature.[16–18] In this regard, Agresti et al.[19] incorporated the MXene into perovskite solar cells to tune the work function and band alignment, which led to a 26% increase in power conversion efficiency (PCE). Lemos et al.[20] reported that $Ti_3C_3T_x$ MXene/TiO_2 photoanodes showed 20% higher PCE than bare TiO_2 photoanodes, as highly conductive MXene provides a straight path for charge carries and prevents the recombinations at the photoanode/electrolyte interface in DSSCs. Another work explored CuSe/MXene as a counter electrode in QDSSC, as MXene has a larger specific surface area for higher catalytic activity and better charge transfer.[21] In our previous report,[6] the partial oxidation of MXene into large-sized TiO_2 nanostructures facilitated effective light scattering and enhanced electron transport through the photoanode. Numerous other studies[22–24] have explored the incorporation of noble metals into TiO_2 to generate metal nanoparticles that exhibited the LSPR effect. Nevertheless, the direct contact between the metal nanoparticles and the electrolyte induces corrosion, thereby compromising the stability of our device. Additionally, metal nanoparticles exhibit the Fano effect through the destructive interference of light, reducing light absorption.[25] To address this concern, the ion implantation technique is considered as more precise and controllable, and favors the atomic-level doping of atoms in the TiO_2 lattice rather than the formation of metal nanoparticles. In this context, Bhullar et al.[26] implanted metal ions into a TiO_2 photoanode to enhance light absorption and reduce recombination by the creation of new trap states.

Taking into account the above, the present work focuses on the implantation of Ag ions in a MXene/TiO_2-based photoanode for QDSSCs. First, MXene was incorporated into TiO_2 to enhance the light scattering and improve the electron transport. Then the photoanodes were implanted with Ag ions via a low-energy ion beam at fluence rates of 5×10^{12}, 5×10^{13}, 5×10^{14}, and 5×10^{15} ions-cm^{-2}. The crystallinity of the samples was studied by x-ray diffraction (XRD) and Raman spectroscopy. The substitution doping of Ag was confirmed by x-ray photoelectron spectroscopy (XPS), and the enhancement in absorption and reduction in recombinations due to the creation of new impurity states was confirmed by UV-visible and photoluminescence (PL) spectroscopy. Ultimately, the QDSSC device fabricated with Ag implanted at a fluence of 5×10^{14} ions-cm^{-2} demonstrated a 58% improvement in PCE compared to the reference QDSSC. This enhancement is attributed to the higher light absorption and reduced number of recombinations in the photoanode with Ag implantation.

Materials and Methods

Materials

Titanium(IV) isopropoxide (TTIP), hydrofluoric acid, cadmium acetate dihydrate ($Cd(CH_3COO)_2{\cdot}2H_2O$), zinc acetate dihydrate ($Zn(CH_2COO)_2{\cdot}2H_2O$), sodium sulfide nonahydrate ($Na_2S{\cdot}9H_2O$), methanol, acetone, isopropanol, fluorine-doped tin oxide (FTO), sulfur (S), sodium hydroxide (NaOH), and dimethyl sulfoxide (DMSO) were all purchased from Merck, India. The brass sheet was purchased from Alfa Aesar, and TiO_2 paste (T/SP, Ti-nanoxide) was purchased from Solaronix SA, Switzerland. MAX (M → early transition metal, A →13 and 14 group elements, and X → carbon and/or nitrogen) (Ti_3AlC_2) powder was procured from Nanoshel, USA. All chemicals were used as received without further purification.

MXene Synthesis

MAX powder (3 g) was slowly added to hydrofluoric acid (60 ml) in a Teflon beaker and stirred for 48 h at room temperature for Al etching. Then, the obtained slurry was centrifuged at 3500 rpm for the removal of Al and washed several times with deionized (DI) water using vacuum filtration until a pH of 6 was attained. Afterwards, the dispersion was dried in an oven at 60°C. Further, the obtained powder was dissolved in DMSO for intercalation and stirred for 24 h. For the delamination of MXene sheets, the obtained solution was probe-sonicated for 1 h. Finally, to obtain MXene powder, the slurry was again filtered and dried at 60°C for 12 h.

Preparation of Unimplanted MXene/TiO_2 and Ag-Implanted MXene/TiO_2 -Based Photoanodes

The preparation steps of photoanodes are shown in Fig. 1a. First, the FTO substrates (1.5 × 1.5 cm) were patterned and cleaned by ultrasonication in various steps: soap solution, DI water, acetone, methanol, and propanol for 15 min each. Then, the compact layer of TTIP was spin-coated onto the pre-cleaned FTO substrates as discussed in our previous work.[6] After that, MXene/TiO_2 photoanodes were prepared by mixing 30 wt.% of MXene in TiO_2 paste and doctor bladed on the prepared substrates followed by annealing at 450°C for 30 min. These photoanodes were then implanted with Ag ions at the low-energy negative ion beam facility at IUAC, New Delhi, India, at an energy of 80 keV with fluence rates of 5×10^{12}, 5×10^{13}, 5×10^{14}, and 5×10^{15} ions-cm^{-2}, designated as Ag_1, Ag_2, Ag_3, and Ag_4, respectively. The unimplanted photoanode was prepared for reference and named Ag_0. XRD patterns were recorded for the prepared samples using a PANalytical XRD instrument equipped with Cu Kα radiation, and Raman spectra were recorded on a Renishaw micro-Raman spectrometer with argon laser at 514 nm wavelength. To determine the elemental composition of the prepared samples, XPS was performed using an ULVAC PHI VersaProbe III instrument with a binding energy (BE) range of 1–1000 eV. The morphology of the samples was studied by field-emission scanning electron microscopy (FESEM) on a Carl Zeiss Supra 55 instrument. Next, CdS QDs were loaded on photoanodes via successive ionic layer adsorption and reaction (SILAR). Briefly, the samples were immersed in a 0.1 M $Cd(CH_3COO)_2 \cdot 2H_2O$ for 1 min and washed with ethanol and then dipped into a solution of 0.1 M $Na_2S \cdot 9H_2O$ and washed with respective solvent. This process was repeated for seven SILAR cycles. Additionally, a passivation layer of ZnS was deposited by SILAR for three cycles using 0.1 M $Zn(CH_2COO)_2 \cdot 2H_2O$ and 0.1 M $Na_2S \cdot 9H_2O$ solutions. UV-visible spectra were then recorded for the unimplanted photoanode loaded with CdS QDs and the photoanode implanted with Ag using a Shimadzu UV–Vis–NIR 3600 spectrometer within the range of 300−700 nm. The PL spectra were also recorded using a PerkinElmer LS-55 spectrometer.

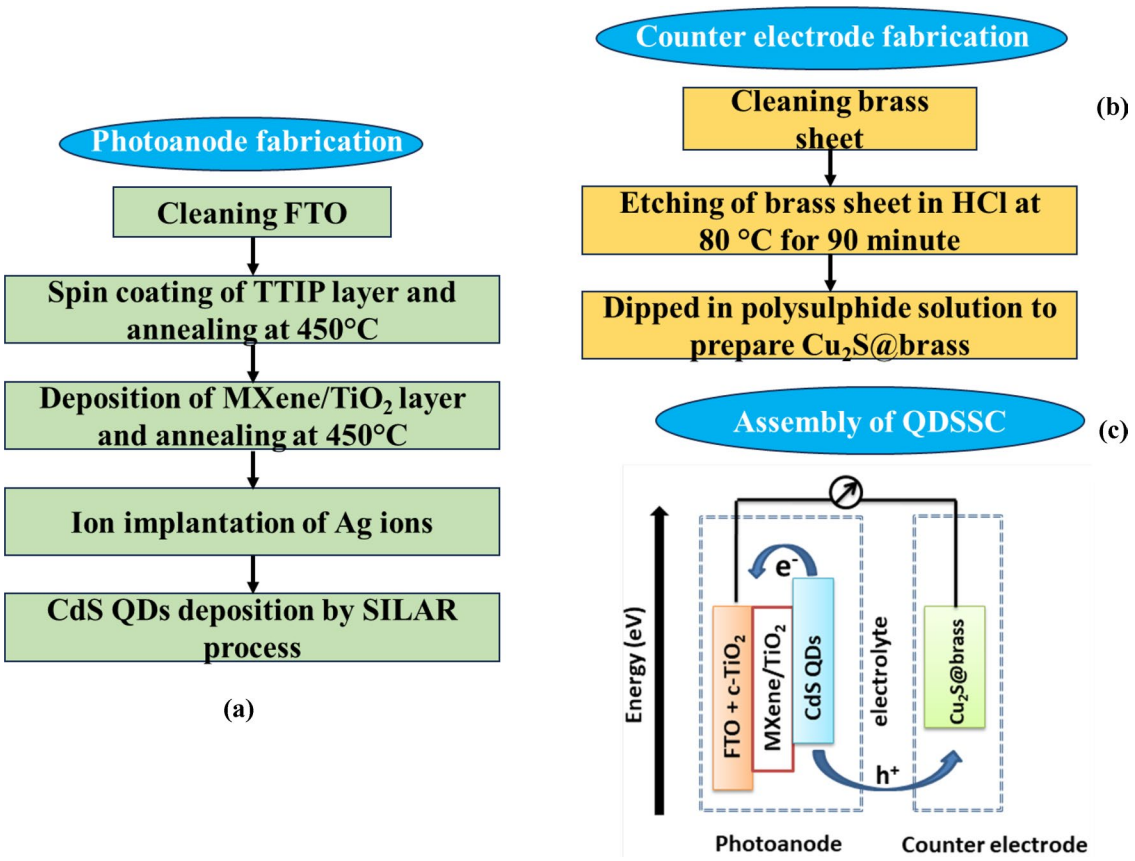

Fig. 1 Flowchart showing the (a) fabrication of the photoanode, (b) fabrication of the counter electrode, and (c) assembly of the QDSSC.

QDSSC Fabrication

The Cu_2S@brass-based CE was prepared by etching of a brass sheet in HCl at 80°C for 90 min, then dipping it in a polysulfide electrolyte for 10 min (Fig. 1b). Finally, QDSSCs were prepared by sandwiching the prepared photoanodes and CE and injecting the polysulfide electrolyte between them (Fig. 1c). The prepared QDSSCs were illuminated under a solar simulator of 100 mW cm^{-2} (OAI TriSOL) of intensity 1.5 G AM, and a Keithley 2400 SourceMeter was used to record the photovoltaic characteristics. Electrochemical impedance spectroscopy (EIS) was performed using an Autolab potentiostat/galvanostat (PGSTAT302) at forward-biased open-circuit voltage within the frequency range of 0.01 Hz to 1 MHz, and Nyquist plots were fitted using EC-Lab v.11.21 software with $\chi^2 < 0.001$.

Results and Discussion

The morphology of the pristine MXene, MXene annealed at 450°C, and the MXene/TiO_2 photoanode were analyzed by FESEM. Figure 2a shows the successful formation of 2D layered sheet-like morphology of pristine MXene. Figure 2b presents the morphology of pristine MXene when annealed at 450°C, where the growth of large-sized TiO_2 nanostructures (100–200 nm) can be seen on the surface of MXene, leading to the oxidization of the MXene surface. Figure 2c presents the MXene/TiO_2 hybrid-based photoanode, when TiO_2 paste mixed with MXene was annealed at 450°C, showing the formation of an m-TiO_2 layer with nanoparticles 15-20 nm in size on the oxidized MXene surface. Notably, the morphology (Fig. 2c) of the MXene-incorporated TiO_2-based photoanode with m-TiO_2 nanoparticles (15–20 nm) accompanied by the large-sized surface-oxidized MXene nanostructure is beneficial for efficient light scattering and hence leads to enhanced light absorption.

The effect of Ag implantation on the surface morphology of the samples was examined by FESEM as shown in Fig. 3. Samples at lower fluence (Ag_1 and Ag_2) show (Fig. 3a and b) almost identical morphology to that of the unimplanted MXene/TiO_2 sample, whereas with increasing fluence, the Ag_3 sample exhibits (Fig. 3c) a large grain size due to the coalescence of the MXene/TiO_2 nanoparticles, leading to a smaller number of grain boundaries, enhancing the charge transport. Conversely, for the Ag_4 sample (Fig. 3d), the high fluence led to distortion of the mesoporous structure, resulting in decreased QD loading and hence reduced light absorption.

XRD patterns of pristine MXene, annealed MXene, and MXene/TiO_2 -based samples are illustrated in Fig. 4. Sharp peaks of pristine MXene were observed at 9.28° (002), 18.49° (004), 35.97° (103), 41.94° (105), and 60.61° (109), confirming the successful formation of MXene nanosheets upon etching as shown in Fig. 4a.[27] On annealing at 450 °C, MXene becomes partially oxidized to TiO_2, as evident from mixed peaks of MXene and an anatase TiO_2 phase. Furthermore, unimplanted and annealed MXene/TiO_2-based samples exhibit sharp peaks at 25.14°, 37.56°, 47.85°, 53.79°, 54.89°, 61.33°, and 62.57° corresponding to (101), (004), (200), (105), (211), (213), and (204) planes of anatase TiO_2 (JCPDS no. 21-1272), whereas small peaks at 35.97° and 41.94° corresponding to oxidized MXene upon annealing. Along with this, diffraction peaks of FTO substrate were also observed.[28] Moreover, Ag-implanted MXene/TiO_2-based samples show similar XRD spectra (Fig. 4b) to the unimplanted MXene/TiO_2-based sample, but a corresponding decrease in the intensity of the peaks belonging to MXene was observed which further disappeared at high fluence (Ag_4), attributed to the oxidation of the MXene due to implantation. Additionally, in the XRD spectra of the Ag-implanted MXene/TiO_2-based samples, the peaks corresponding to Ag were not found, which could be due to

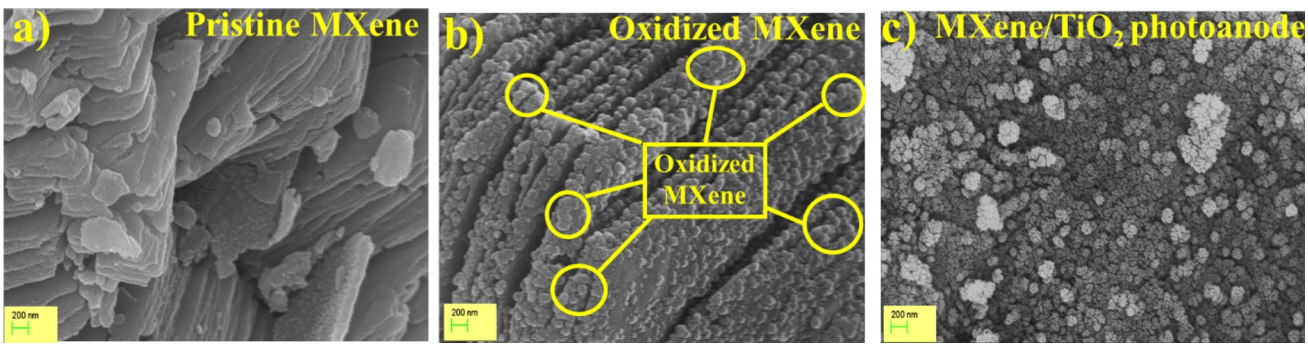

Fig. 2 FESEM images of (a) pristine MXene, (b) oxidized MXene, and (c) MXene/TiO_2-based sample doctor-bladed onto FTO substrate.

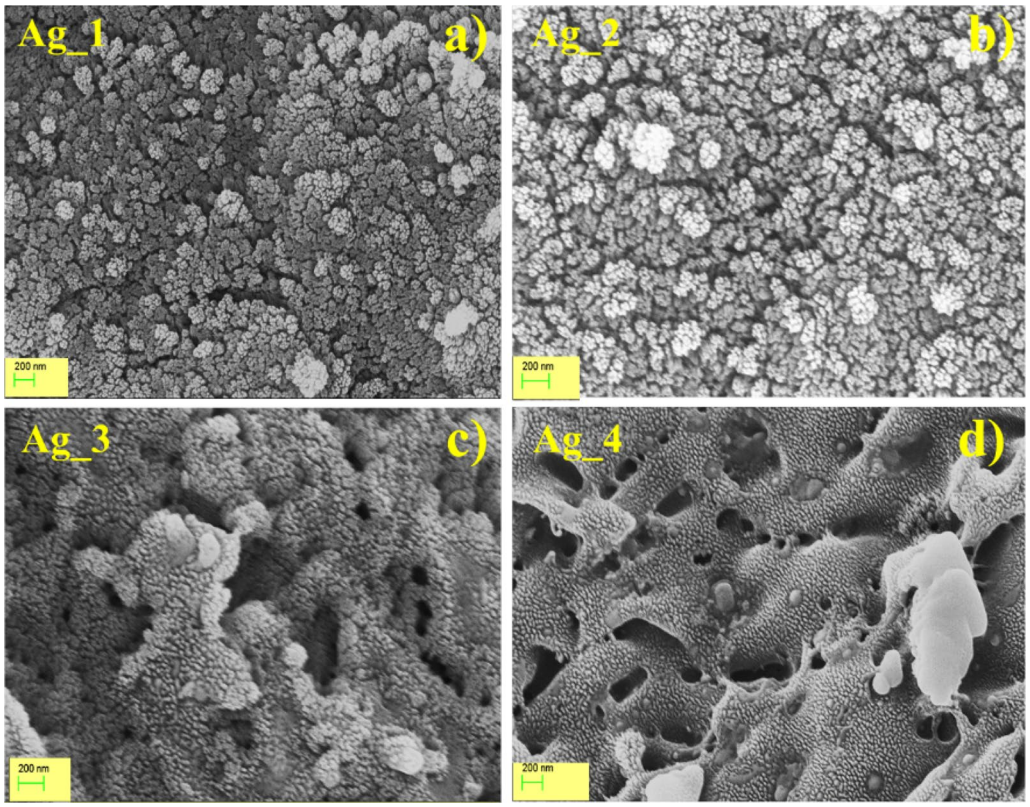

Fig. 3 (a–d) FESEM images of Ag-implanted (Ag_1, Ag_2, Ag_3, and Ag_4) MXene/TiO_2 samples.

the low concentration or due to the solubility of Ag within the TiO_2 matrix.

The Raman spectra of MXene, annealed MXene, and MXene/TiO_2-based samples were studied and the results are shown in Fig. 5. Raman spectra of MXene (Fig. 5a) represent mainly five in-plane and out-of-plane vibrational bands of MXene around 128 cm^{-1} ($\omega_1(E_g)$), 207 cm^{-1} ($\omega_2(A_{1g})$), 365 cm^{-1} (ω_5(Eg)), 633 cm^{-1} (ω_4(Eg)), and 412 cm^{-1} ($\omega_3(A_{1g})$).[29] After annealing at 450°C, Raman spectra show bands corresponding to MXene and anatase TiO_2 owing to the partial oxidation of MXene, which is in accord with XRD results. Furthermore, an unimplanted MXene/TiO_2-based sample (Fig. 5a) shows four main Raman-active bands at 145 cm^{-1} (E_g), 399 cm^{-1} (B_{1g}), 518 cm^{-1} (A_{1g}), and 640 cm^{-1} (E_g) belonging to anatase TiO_2 along with a small band around 207 cm^{-1} ($\omega_2(A_{1g})$) corresponding to MXene.[30] Moreover, implanted samples (Fig. 5b) show Raman bands of anatase TiO_2 as well as MXene, but with increasing fluence, the band ($\omega_2(A_{1g})$) corresponding to MXene decreases, which is attributed to the oxidation of MXene with implantation. Again, here, no band corresponding to Ag is detected in the Raman spectra due to the solubility of Ag in TiO_2, which is in accord with XRD results.

XPS analysis was conducted to determine the elemental composition and to assess the interaction between the implanted Ag and TiO_2. In Fig. 6a–e, the survey spectra of both unimplanted and Ag-implanted samples reveal the presence of Ti, O, and C in the samples. Notably, the absence of discernible peaks corresponding to Ag in the survey spectra could be due to the low concentration of implanted Ag in the samples. The atomic % of different elements calculated from their core-level spectra are tabulated in Table I. The core-level spectra for Ag_3 and Ag_4 are illustrated in Fig. 7, where Ag_3 exhibits (Fig. 7a) two distinct peaks at 368 eV (Ag-$3d_{5/2}$) and 374 eV (Ag-$3d_{3/2}$) confirming the presence of Ag^+ ions,[31] which can generate the defects in the MXene/TiO_2 lattice within the valance and conduction bands.[26] These new defect states can increase the light absorption of the photoanode towards higher wavelengths which might act as charge separation sites to minimize charge recombinations. In contrast, at higher fluence for the Ag_4 sample (Fig. 7b), the peaks can be deconvoluted into four peaks at 368.3 eV and 374.3 eV corresponding to Ag^+ ions, and at 368.8 eV and 375 eV corresponding to metallic Ag,[32] which may act as a charge recombination center and degrade device performance.

The core-level spectra of Ti-2*p* (Fig. 8a–e), depicts two discernible peaks at 458 eV (Ti-$2p_{3/2}$) and 464 eV (Ti-$2p_{5/2}$). Subsequent deconvolution of each peak revealed another two distinct sub-peaks at 458.4 eV and 464.2 eV, corresponding

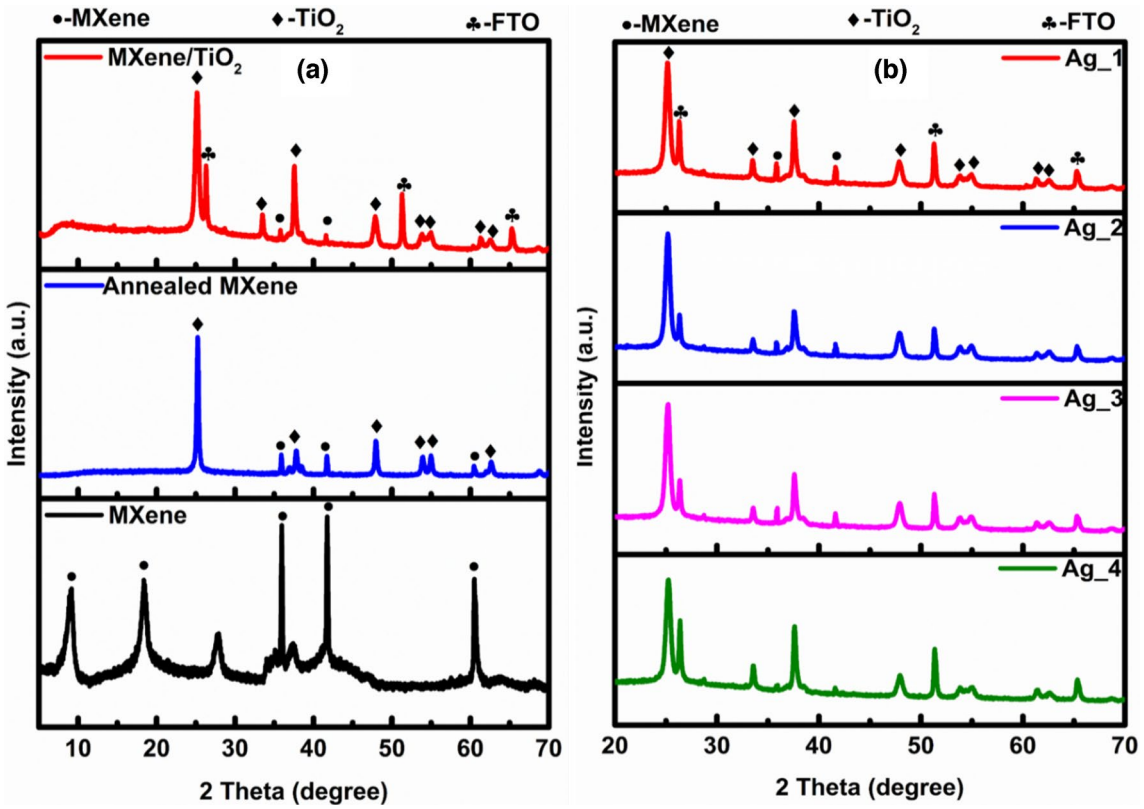

Fig. 4 (a) XRD patterns of MXene, annealed MXene, and unimplanted MXene/TiO_2-based samples, (b) XRD patterns of Ag implanted MXene/TiO_2-based samples.

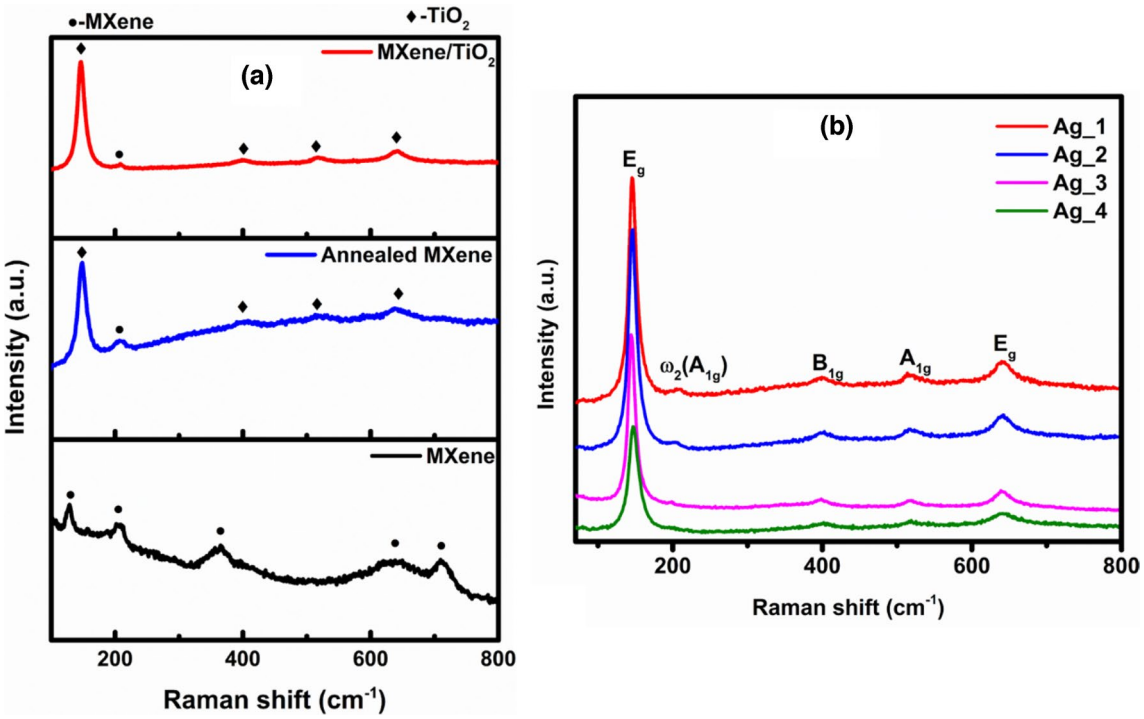

Fig. 5 (a) Raman spectra of MXene, annealed MXene, and unimplanted MXene/TiO_2-based samples, (b) Raman spectra of Ag-implanted MXene/TiO_2-based samples.

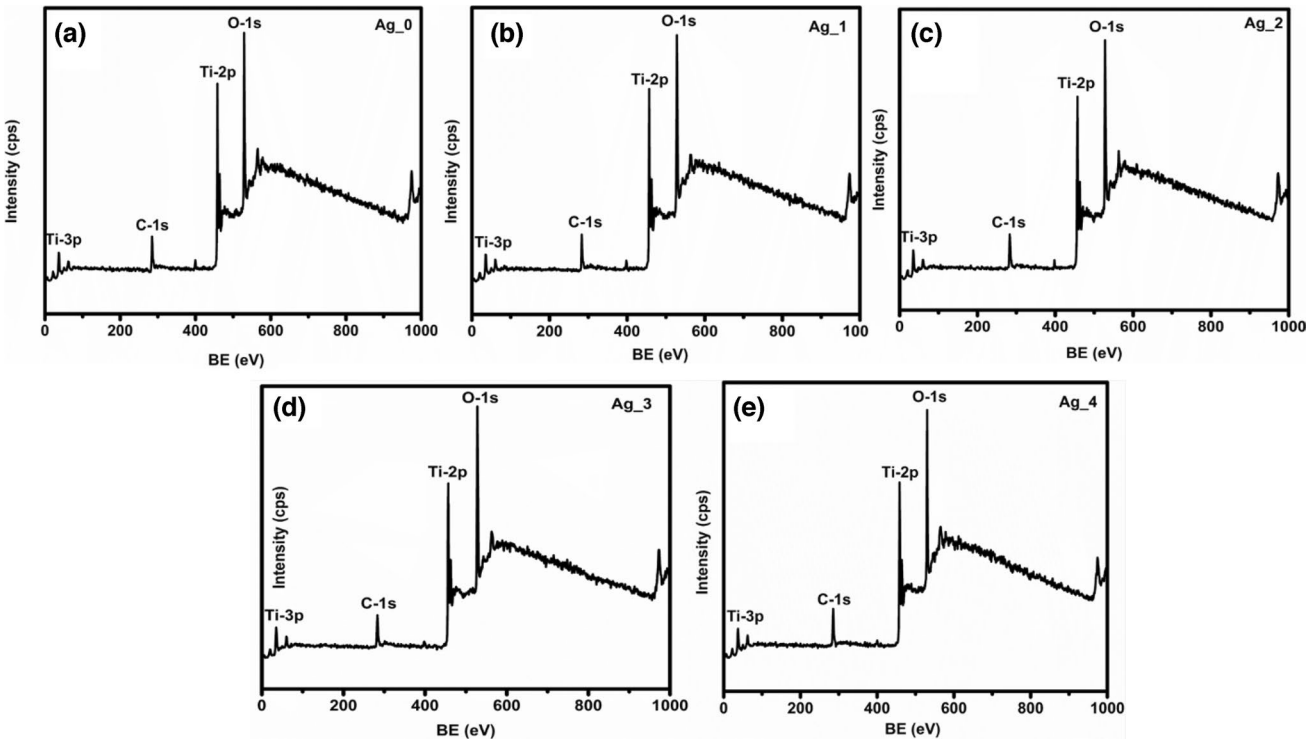

Fig. 6 (a–e) Survey spectra of unimplanted (Ag_0) MXene/TiO_2 and Ag implanted (Ag_1, Ag_2, Ag_3, and Ag_4) MXene/TiO_2 samples.

Table I Atomic % of Ti, O, and Ag present in Ag implanted MXene/TiO_2 samples

Sample	Ti	O	Ag
Ag_1	31.74	68.26	–
Ag_2	30.34	69.66	–
Ag_3	29.36	70.58	0.06
Ag_4	28.09	71.80	0.11

to Ti^{4+}, whereas 457.6 eV and 462.4 eV belong to Ti^{3+} oxidation states.[33] The Ti^{4+}/Ti^{3+} ratio was calculated from their respective peak areas for pristine and optimized samples. For the Ag_0 sample, the Ti^{4+}/Ti^{3+} ratio is 6.62, and after the Ag implantation (Ag_3), it was increased to 9.33, resulting from the oxidation of MXene to TiO_2 with implantation resulting from the fast and local temperature variation of the surface.[34]

The photovoltaic characteristics of fabricated QDSSCs of unimplanted MXene/TiO_2 and Ag-implanted MXene/TiO_2-based photoanodes are shown in Fig. 9a, and corresponding photovoltaic parameters are compiled in Table II. The values of J_{SC} exhibit an obvious increase with implantation from 8.14 mA/cm^2 (Ag_0) to 9.24 mA/cm^2 (Ag_1), 10.58 mA/cm^2 (Ag_2), and reaching a maximum up to 11.56 mA/cm^2 for the Ag_3 sample-based QDSSC. Nevertheless, in the case of Ag_4, there was a noticeable decrease in the J_{SC} value, reducing to 9.93 mA/cm^2.

To explore the reason for this J_{SC} trend, UV-visible spectra of unimplanted and Ag-implanted samples with CdS QDs-loaded photoanodes were recorded as shown in Fig. 9b. It is observed that the absorption edge lies within 400–500 nm and absorption increases (around 420 nm) with Ag ion implantation, owing to the formation of new defect states between the valance band and conduction band of TiO_2. In the spectra, optimized Ag_3 shows maximum absorption with the highest J_{SC} value of 11.56 mA/cm^2; however, the decrease in J_{SC} at the highest fluence (Ag_4) can be attributed to the decrease in light absorption by the photoanode, which results from the distorted mesoporous structure at higher fluence levels, as observed in the FESEM analysis, could resulting in the diminution of QD loading.

Further, EIS was conducted under forward-biased open-circuit voltage conditions to investigate electron transport mechanisms and charge recombinations. The Nyquist plots, fitted with an equivalent circuit, are illustrated in Fig. 10a. Here, two semicircles in the Nyquist plots were observed, first at a lower frequency range corresponding to the charge transfer resistance (R_1) at the electrolyte/CE interface, and at an intermediate frequency associated with charge transfer resistance (R_2) at the photoanode/electrolyte interface. The resistance R_1 exhibits nearly the same value across all QDSSCs, as a similar CE was used for constructing each device. Table II provides the R_2 values calculated from

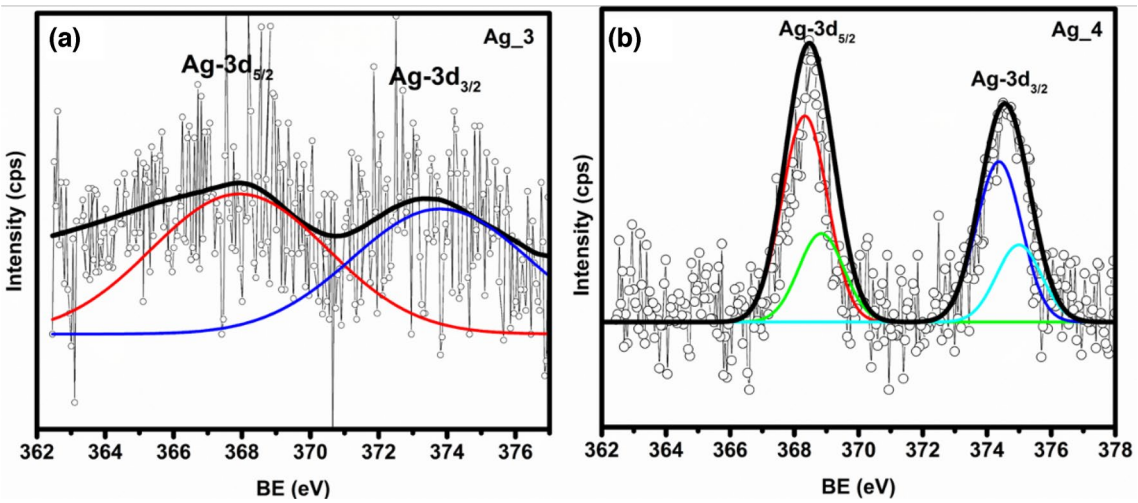

Fig. 7 (a, b) High-resolution core-level Ag-3d XPS spectra of Ag implanted (Ag_3 and Ag_4) MXene/TiO_2 samples.

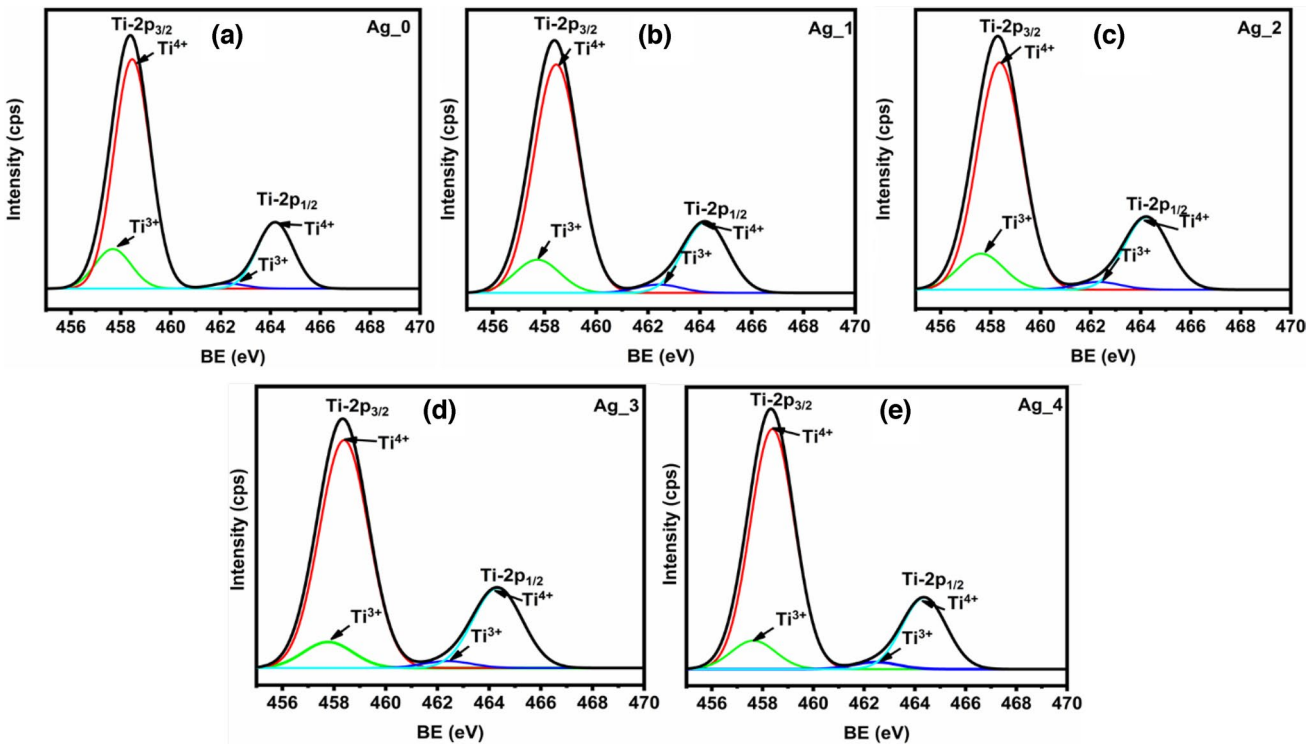

Fig. 8 (a) High-resolution core-level Ti-2p XPS spectra of unimplanted (Ag_0) MXene/TiO_2 and (b–e) high-resolution core-level Ti-2p XPS spectra of Ag-implanted (Ag_1, Ag_2, Ag_3, and Ag_4) MXene/TiO_2 samples.

Nyquist plots for all fabricated QDSSCs. The effect of Ag ion implantation on MXene/TiO_2-based samples was also examined using Nyquist plots. It was found that as the fluence increased from 5×10^{12} to 5×10^{14} ions-cm^{-2}, the corresponding R_2 value decreased from 163.1 to 30.7 ohm-cm^2, respectively. Conversely, on further increasing the fluence (Ag_4), the R_2 value again increases to 127.1 ohm-cm^2, suggesting a higher number of recombinations. To further confirm the reduction in charge recombinations, before and after implantation of MXene/TiO_2-based samples, PL

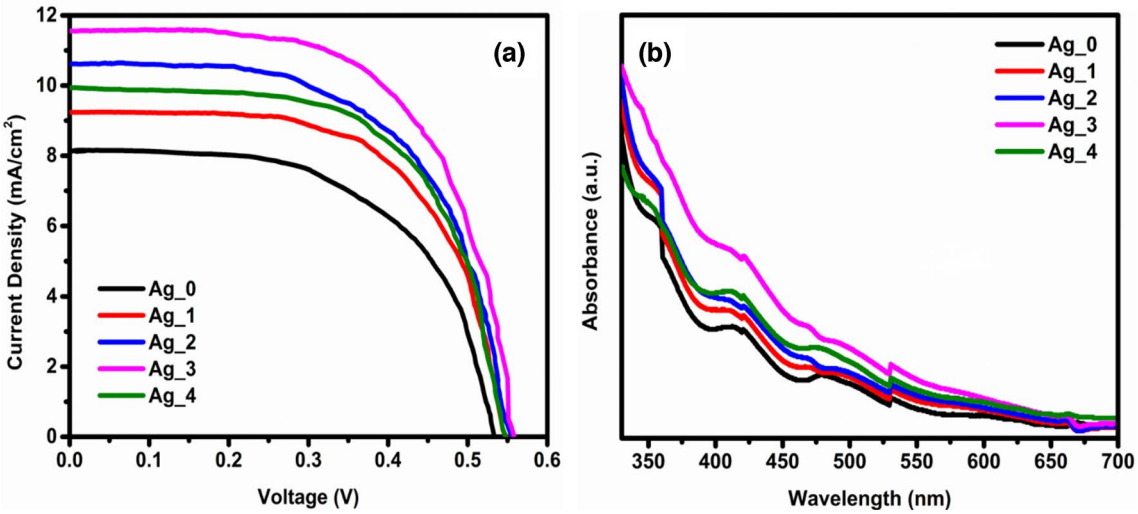

Fig. 9 (a) Photovoltaic characteristics, and (b) UV-visible spectra of unimplanted (Ag_0) MXene/TiO_2 and Ag-implanted (Ag_1, Ag_2, Ag_3, and Ag_4) MXene/TiO_2 samples.

Table II Photovoltaic parameters of unimplanted and Ag-implanted QDSSCs

QDSSC	J_{SC} (mA/cm^2)	V_{OC} (V)	FF	PCE (%)	R_2 (ohm-cm^2)
Ag_0	8.14	0.53	0.57	2.48	163.1
Ag_1	9.24	0.54	0.62	3.11	153.6
Ag_2	10.58	0.55	0.60	3.46	118.7
Ag_3	**11.56**	**0.55**	**0.62**	**3.94**	**30.7**
Ag_4	9.93	0.55	0.61	3.34	127.1

Bold indicates optimized parameters of fabricated cell

spectroscopy was employed (Fig. 10b). It is widely recognized that the PL intensity correlates directly with the number of recombinations; the lower the PL intensity, the lower the number of recombinations. The PL spectra for all samples revealed two broad peaks situated at 420 nm and 519 nm attributed to radiative recombination arising from surface-trapped excitons and free electrons and holes confined around oxygen vacancies, respectively.[34] Among all the samples, the Ag_3 sample exhibited the lowest PL intensity, which is direct evidence of reduced charge recombination, due to the creation of new charge trap states between the valence band and conduction band of TiO_2. Moreover, the higher PL intensity of the Ag_4 sample indicates an increased number of recombinations at the higher fluence, which could be due to the formation of metallic Ag which acts as a recombination center. Thus, as a whole, QDSSCs based on Ag_3 achieved the highest overall PCE of 3.94%, which is 58% greater than that of the Ag_0 sample (pristine MXene/TiO_2), attributed to higher light absorption and low charge recombinations.

Conclusion

In conclusion, MXene/TiO_2-based photoanodes were successfully fabricated with partial oxidation of MXene into large TiO_2 nanoparticles (100–200 nm). Upon annealing, they were found to be immersed within m-TiO_2 nanoparticles, which facilitates efficient light scattering. Afterwards, Ag implantation was performed for as-prepared MXene/TiO_2-based samples at variable fluence (5×10^{12}, 5×10^{13}, 5×10^{14}, and 5×10^{15} ions-cm^{-2}), and utilizing these photoanodes, respective QDSSCs were fabricated. Among all of these, the QDSSC prepared with Ag implanted at fluence of 5×10^{14} ions-cm^{-2} (Ag_3) exhibited a maximum J_{SC} value of 11.56 mA/cm^2 with maximum PCE of 3.94%, which is 58% greater than that of the unimplanted MXene/TiO_2-based QDSSC. This enhancement in J_{SC} value is attributed to enhanced light absorption and reduced number of recombinations owing to the formation of new charge trap states between the conduction band and valence band, which was verified by UV-visible, PL, and EIS.

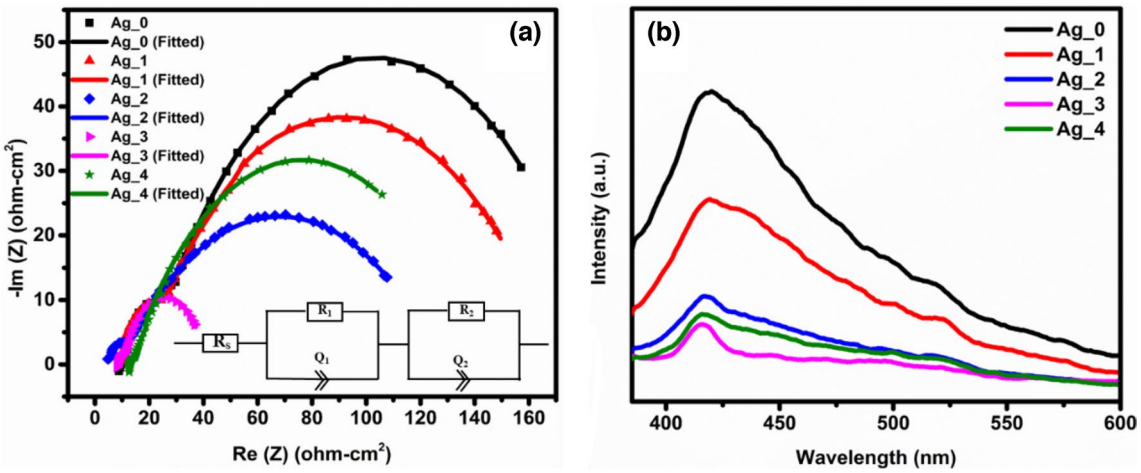

Fig. 10 (a) Nyquist plots, (b) PL spectra of QDSSCs prepared with unimplanted (Ag_0) MXene/TiO_2 and Ag-implanted (Ag_1, Ag_2, Ag_3, and Ag_4) MXene/TiO_2 samples.

Acknowledgments The authors are grateful to IUAC, New Delhi, India, for providing the beam time facility and financial assistance under project No. UFR-69304.

Data availability Data will be made available on request.

Conflict of interest The authors have no conflicts to disclose.

References

1. I. Singh, V. Bhullar, and A. Mahajan, Interfacial engineering of a TiO_2 photoanode via graphene nanoribbons for efficient quantum-dot-sensitized solar cells and photoelectrochemical water splitting. *Energy Fuels* 37, 15054 (2023).
2. N. Singh, V. Murugadoss, S. Nemala, S. Mallick, and S. Angaiah, Cu2ZnSnSe4 QDs sensitized electrospun porous TiO_2 nanofibers as photoanode for high performance QDSC. *Sol. Energy* 171, 571 (2018).
3. N.T. Chung, P.T. Nguyen, H.T. Tung, and D.H. Phuc, Quantum Dot sensitized solar cell: photoanodes, counter electrodes, and electrolytes. *Mol.* 26(9), 2638 (2021).
4. S.S. Rayalu, D. Jose, M.V. Joshi, P.A. Mangrulkar, K. Shrestha, and K. Klabunde, Photocatalytic water splitting on Au/TiO_2 nanocomposites synthesized through various routes: enhancement in photocatalytic activity due to SPR effect. *Appl. Catal. B Environ.* 142–143, 684 (2013).
5. M.A.K.L. Dissanayake, H.K.D.W.M.N. Divarathna, C.B. Dissanayake, G.K.R. Senadeera, P.M.P.C. Ekanayake, and C.A. Thotawattage, An innovative TiO_2 nanoparticle/nanofibre/nanoparticle, three layer composite photoanode for efficiency enhancement in dye-sensitized solar cells. *J. Photochem. Photobiol. A.* 322–323, 110 (2016).
6. I. Singh, V. Bhullar, D. Devi, F. Singh, S. Chopra, A. Krishna Debnath, D. Kumar Aswal, and A. Mahajan, Au ion beam engineered MXene incorporated TiO_2 photoanodes for quantum dot sensitized solar cells. *Mat. Sci. Eng. B.* 290, 116342 (2023).
7. V. Bhullar, S. Sardana, and A. Mahajan, Size modeling of TiO_2 nanofibers for efficient TiO_2 sensitized mesoscopic solar cells. *Sol. Energy* 230, 177 (2021).
8. R. Zhou, Q. Zhang, E. Uchaker, L. Yang, N. Yin, Y. Chen, M. Yin, and G. Cao, Photoanodes with mesoporous TiO_2 beads and nanoparticles for enhanced performance of CdS/CdSe quantum dot co-sensitized solar cells. *Electrochim. Acta* 135, 284 (2014).
9. M. Marandi, P. Talebi, and L. Moradi, Co-application of TiO_2 nanoparticles and randomly directed TiO_2 nanorods in the photoelectrode of the CdS: Mn quantum dots sensitized solar cells and optimization of the doping for the efficiency improvement. *Opt. Mater.* 94, 224 (2019).
10. T. Toyoda and Q. Shen, Quantum-dot-sensitized solar cells: effect of nanostructured TiO_2 morphologies on photovoltaic properties. *J. Phys. Chem. Lett.* 3, 1885 (2012).
11. A. Tanvi, R.K. Mahajan, S. Bedi, V. Kumar, A. Saxena, D.K. Singh, and Aswal, Broadband enhancement in absorption cross-section of N719 dye using different anisotropic shaped single crystalline silver nanoparticles. *RSC Adv.* 6, 48064 (2016).
12. N. Kaur, V. Bhullar, D.P. Singh, and A. Mahajan, Bimetallic implanted plasmonic photoanodes for TiO_2 sensitized third generation solar cells. *Sci. Rep.* 10, 7657 (2020).
13. V. Bhullar, D. Devi, F. Singh, S. Chopra, A.K. Debnath, D.K. Aswal, and A. Mahajan, Ion implanted substitutionally dispersed Au in TiO_2 nanostructures for efficient and stable dye sensitized solar cells. *Opt. Mater.* 132, 112800 (2022).
14. T. Raguram and K.S. Rajni, Synthesis and characterisation of Cu - doped TiO_2 nanoparticles for DSSC and photocatalytic applications. *Int. J. Hydrogen Energy* 47, 4674 (2022).
15. Y.X. Dong, X.L. Wang, E.M. Jin, S.M. Jeong, B. Jin, and S.H. Lee, One-step hydrothermal synthesis of Ag decorated TiO_2 nanoparticles for dye-sensitized solar cell application. *Renew. Energy* 135, 1207 (2019).
16. Z. Yu, W. Feng, W. Lu, B. Li, H. Yao, K. Zeng, and J. Ouyang, MXenes with tunable work functions and their application as electron- and hole-transport materials in non-fullerene organic solar cells. *J. Mater. Chem. A.* 7, 11160 (2019).
17. H.-C. Fu, V. Ramalingam, H. Kim, C.-H. Lin, X. Fang, H.N. Alshareef, and J.-H. He, MXene-contacted silicon solar cells with 11.5% efficiency. *Adv. Energy Mater.* 9, 1900180 (2019).

18. C. Dall'Agnese, Y. Dall'Agnese, B. Anasori, W. Sugimoto, and S. Mori, Oxidized Ti_3C_2 MXene nanosheets for dye-sensitized solar cells. *New J. Chem.* 42, 16446 (2018).
19. A. Agresti, A. Pazniak, S. Pescetelli, A. Di Vito, D. Rossi, A. Pecchia, M. Auf der Maur, A. Liedl, R. Larciprete, D.V. Kuznetsov, D. Saranin, and A. Di Carlo, Titanium-carbide MXenes for work function and interface engineering in perovskite solar cells. *Nat. Mater.* 18, 1228 (2019).
20. H.G. Lemos, R.M. Ronchi, G.R. Portugal, J.H.H. Rossato, G.S. Selopal, D. Barba, E.C. Venancio, F. Rosei, J.T. Arantes, and S.F. Santos, Efficient $Ti_3C_2T_x$ MXene/TiO_2 hybrid photoanodes for dye-sensitized solar cells. *ACS Appl. Energy Mater.* 5, 15928 (2022).
21. Y. Chen, D. Wang, Y. Lin, X. Zou, and T. Xie, In suit growth of CuSe nanoparticles on MXene (Ti3C2) nanosheets as an efficient counter electrode for quantum dot-sensitized solar cells. *Electrochim. Acta* 316, 248 (2019).
22. I. Zada, W. Zhang, W. Zheng, Y. Zhu, Z. Zhang, J. Zhang, M. Imtiaz, W. Abbas, and D. Zhang, The highly efficient photocatalytic and light harvesting property of Ag-TiO2 with negative nanoholes structure inspired from cicada wings. *Sci. Rep.* 7, 17277 (2017).
23. Z. Du, F. Yin, D. Han, S. Mao, J. Wang, A.R. Aleem, Z. Pan, and J. Tang, Plasmonic effect with tailored Au@TiO2 nanorods in photoanode for quantum dot sensitized solar cells. *ACS Appl. Energy Mater.* 2, 5917 (2019).
24. H. Zhao, F. Huang, J. Hou, Z. Liu, Q. Wu, H. Cao, Q. Jing, S. Peng, and G. Cao, Efficiency enhancement of quantum dot sensitized TiO_2/ZnO nanorod arrays solar cells by plasmonic Ag nanoparticles. *ACS Appl. Mater. Interfaces* 8, 26675 (2016).
25. Z.S. Seddigi, S.A. Ahmed, S. Sardar, and S.K. Pal, Carbonate doping in TiO_2 microsphere: The key parameter influencing others for efficient dye sensitized solar cell. *Sci. Rep.* 6, 23209 (2016).
26. V. Bhullar and A. Mahajan, Cu implanted TiO2 based dye sensitized solar cells: Unraveling the effect of doping mechanism and type of metal ion on the photovoltaic properties. *Sol. Energy* 254, 8 (2023).
27. A.K. Navjyoti, V. Sharma, A.K. Sharma, V. Debnath, and A. Saxena, Mahajan, MXene supported nickel-cobalt layered double hydroxide as efficient bifunctional electrocatalyst for hydrogen and oxygen evolution reactions. *ACS J. Alloy. Compd.* 939, 168779 (2023).
28. M. Pogorielov, K. Smyrnova, S. Kyrylenko, O. Gogotsi, V. Zahorodna, and A. Pogrebnjak, MXenes—A new class of two-dimensional materials: structure, properties and potential applications. *Nanomaterials* 11(12), 3412 (2021).
29. L. Zhang, W. Su, Y. Huang, H. Li, L. Fu, K. Song, X. Huang, J. Yu, and C.-T. Lin, In situ high-pressure X-ray diffraction and Raman spectroscopy study of $Ti_3C_2T_x$ MXene. *Nanoscale Res. Lett.* 13, 343 (2018).
30. H. Wang, Y. Wu, J. Zhang, G. Li, H. Huang, X. Zhang, and Q. Jiang, Enhancement of the electrical properties of MXene Ti_3C_2 nanosheets by post-treatments of alkalization and calcination. *Mat. Lett.* 160, 537 (2015).
31. Y. Li, M. Ma, W. Chen, L. Li, and M. Zen, Preparation of Ag-doped TiO_2 nanoparticles by a miniemulsion method and their photoactivity in visible light illuminations. *Mat. Chem. Phys.* 129, 501 (2011).
32. S. Demirci, T. Dikici, M. Yurddaskal, S. Gultekin, M. Toparli, and E. Celik, Synthesis and characterization of Ag doped TiO_2 heterojunction films and their photocatalytic performances. *Appl. Surf. Sci.* 390, 591 (2016).
33. W.-C. Peng, Y.-C. Chen, J.-L. He, S.-L. Ou, R.-H. Horng, and D.-S. Wuu, Tunability of p- and n-channel TiO_x thin film transistors. *Sci. Rep.* 8, 9255 (2018).
34. V. Bhullar, D. Devi, F. Singh, S. Chopra, A.K. Debnath, D.K. Aswal, and A. Mahajan, Ag implanted TiO_2 nanoparticle/nanofibers composites for dye sensitized solar cells applications. *Sol. Energy* 241, 109 (2022).